sustainability

MDPI

Article

Numerical Simulation of Storm Surge Inundation in Estuarine Area Considering Multiple Influencing Factors

Cifu Fu [1,2], Qiuxing Liu [1,2], Yi Gao [1,2], Haijin Cao [2,3] and Sendong Liang [1,2,*]

[1] National Marine Environmental Forecasting Center, Beijing 100081, China; fucf@nmefc.cn (C.F.); lqx@nmefc.cn (Q.L.); gaoyi@nmefc.cn (Y.G.)
[2] Key Laboratory of Marine Hazards Forecasting, Ministry of Natural Resources, Beijing 100081, China; h.cao@hhu.edu.cn
[3] College of Oceanography, Hohai University, Nanjing 210024, China
* Correspondence: liangsd@nmefc.cn

Abstract: With global climate change, the risk of extreme storms and storm surges in estuarine areas is increasing; thus, storm surge inundation research and prediction have become important issues to ensure sustainable development in estuarine areas. The Jitimen estuary in Guangdong Province, China, was chosen as our study area. In this study, a numerical model for simulating storm surge inundation in small regions based on unstructured triangular grids was established, and the model accuracy was validated. The typhoon characteristics in the study area were statistically analyzed based on historical data. Three experimental schemes, involving factors influencing storm surge inundation, such as typhoon landfall location, intensity, and direction, were used to evaluate the differences in the numerical results. The results showed that when the typhoon landfall direction remained unchanged and the highest tide levels at the Sanzao tide gauge station were similar, the differences between the numerical results for the typhoon landfall location and typhoon intensity schemes were less than 5%, and the inundation characteristics were similar. However, when the typhoon location and intensity were unchanged and the highest tide levels at the Sanzao tide gauge station were similar, the numerical results for the typhoon landfall direction scheme significantly differed; this result was caused by the difference in the duration of the high tide level (exceeding 3 m); these results indicated that the topographic characteristics and the typhoon landing direction had a greater impact on storm surge inundation. The results from this study can aid in the prediction of storm surge inundation information for the Jitimen estuary area when the typhoon landing direction and the maximum tide level are known.

Keywords: estuarine area; influencing factors of typhoon; storm surge inundation; numerical simulation; sustainable development

check for updates

Citation: Fu, C.; Liu, Q.; Gao, Y.; Cao, H.; Liang, S. Numerical Simulation of Storm Surge Inundation in Estuarine Area Considering Multiple Influencing Factors. *Sustainability* **2024**, *16*, 2274. https://doi.org/10.3390/su16062274

Academic Editor: Maxim A. Dulebenets

Received: 29 January 2024
Revised: 23 February 2024
Accepted: 7 March 2024
Published: 8 March 2024

Copyright: © 2024 by the authors. Licensee MDPI, Basel, Switzerland. This article is an open access article distributed under the terms and conditions of the Creative Commons Attribution (CC BY) license (https://creativecommons.org/licenses/by/4.0/).

1. Introduction

A storm surge involves local sea level oscillation or a nonperiodic abnormal rise or fall in sea level caused by strong winds and sudden changes in the air pressure associated with the passage of storms such as tropical cyclones, temperate weather systems, and oceanic squall lines. In China, the frequency of storm surge disasters triggered by tropical cyclones, especially low-lying coastal area inundation caused by extreme storm surge events, has threatened societies and economies in coastal areas [1]. In the Pearl River Estuarine area of Guangdong Province, China, the super typhoons Hato and Mangkhut successively made landfall along the coast in 2017 and 2018, leading to widespread storm surge inundations in the coastal cities [2,3], causing tremendous economic losses and threatening the sustainable development of the coastal areas.

In the context of climate change, global sea levels have been rising significantly since the late 19th century; global sea levels rose by approximately 14 cm in the 20th century [4–6].

According to long-term observation data from coastal tide gauge stations, sea levels along the coast of China have also exhibited an upward trend over the past 40 years [7]. Based on simulations using the Coupled Model Intercomparison Project Phase 6 (CMIP6) model, simulations have demonstrated that since the 1980s, climate change has led to a noticeable seasonal shift in the global occurrence of super typhoons [8]. Some studies have shown that under high-emission scenarios, low-lying coastal areas will experience more frequent storm surge disasters due to the rapid rise in sea levels [9]. According to the statistical results from the coastal tide data in China, estuarine areas, such as the Pearl River Estuary, have a high probability of experiencing strong storm surges and are among the regions with the highest risk for storm surge disasters in coastal China [10]. Accordingly, conducting simulation studies and predicting storm surge inundations in estuarine areas have great significance for disaster prevention.

Numerical models for storm surges have matured in terms of grid technology, dynamic frameworks, and parameterization schemes [3,11]. In the past ten years, with the rapid economic and population development in estuarine areas, simulations of storm surge inundation in estuarine areas have attracted the attention of many scholars, who have established fine grids for small regions (50–300 km) along the coast and developed storm surge inundation simulation and forecast models to support storm surge disaster prevention in coastal areas [12–15]. With enhanced computational capabilities, the land resolution in storm surge inundation models has increased from several hundred meters to 10 m, enabling block-level resolution and providing more detailed storm surge inundation simulation results [16,17]. However, considerable computational resources are required.

At the same time, the study of multiple influencing factors of storm surges in estuarine areas has also attracted the attention of many scholars. A numerical model (Delft3D), previously calibrated and validated, was used to simulate the lagoon hydrodynamics under different scenarios combining the mean sea level (MSL) rise and frequent storm surge events; moreover, the numerical results demonstrated that an MSL rise could change vertical zonation and threaten local habitats [18]. When considering spring tides, storm surges, and river inflows under sea-level increases of 0.4 m and 0.9 m, the floodplains in mature estuarine systems may become submerged and experience a considerable increase in inundation depths once a certain threshold in elevation has been exceeded; conversely, immature estuarine systems can experience increases in the relative inundation extent and substantial changes in hydrodynamics such as tidal range and current velocity [19]. A hydrodynamic model (Delft3D-FM) was used to study the flooding from both the coastal and fluvial influences in the Napa River and its interactions with the San Francisco Bay, and the results showed that large tidal amplitudes diminished the storm surge propagation upstream and that phasing between peak fluvial discharge and high tide was important for predicting the locations and occurrences of the highest water levels; additionally, the interactions between tides, river discharges, and storm surges are complex [20]. A high-resolution, unstructured-grid, surge-wave fully coupled model and a hybrid typhoon wind model was used to assesses the highest storm tide hazard level along the coast of Taiwan, and this assessment is important to establishing an early warning of riverine inundation if the occurrence of the highest storm surge coincides with the highest astronomical tide [21]. The Advanced Circulation (ADCIRC) model coupled with the Precipitation-Runoff Modeling System (PRMS) was used to simulate the impact from the three different versions of hurricanes on the Fox Point Hurricane Barrier (FPHB) in the Rhode Island and Narragansett Bay area; moreover, the storm surge resulting from the strongest version during the first landfall exceeded 7 m; this value exceeded the height of the FPHB, and the results all showed that northern Narragansett Bay could be particularly vulnerable to both storm surge- and rainfall-driven flooding, especially if the FPHB suffered a power outage [22]. A range of meteorological, storm track direction, and storm bearing parameters that produced the highest sustained wind speeds were introduced into meteorological conditions, coupled with storm surges, tides, and waves, for the risk assessment of special infrastructure in Delaware Bay, such as nuclear power plants; the simulations resulted in a maximum

stillwater elevation and wave height of 7.5 m and 2.5 m, respectively, which demonstrated that the estimated elevation probability had an annual exceedance of less than 10^{-4} [23].

The above research indicates that multiple factors need to be considered in the study of storm surge inundation in estuarine areas. Due to constraints in the basic data, weather forecasts, and computational capabilities, storm surge inundation forecasting in estuarine areas will become an important focus. To carry out storm surge inundation forecasts in estuarine areas, statistical analyses of the historical storm surge data, disaster data, and typhoon information in the study area need to be carried out and the results used as oceanographic and meteorological background parameters. In addition, the factors influencing storm surge inundations include typhoon landfall intensity, landfall location, landfall direction, typhoon speed, astronomical tide, nearshore waves, and nearshore topography. The existence of many influencing factors can lead to interference in storm surge inundation forecasts. Accordingly, the main focus of this paper includes the establishment of a reasonable method for storm surge inundation experiments and the analysis of the simulation results to highlight the significant factors. The purpose of this study is to reduce the number of factors influencing storm surge inundation through a numerical simulation assessment, establish a lightweight storm surge inundation database in follow-up work, and carry out rapid storm surge inundation forecasting and disaster risk estimation; the results from this study can provide technical support for sustainable development in estuarine areas.

2. Model and Data

2.1. Storm Surge Model

ADCIRC (A (PARALLEL) Advanced Circulation Model For Oceanic, Coastal and Estuarine Waters), a hydrodynamic model developed by Professors Luettich and Westerink based on the finite element method [24], is widely used to simulate currents, tides, and storm surges over complex terrains, such as oceans, coasts, and estuaries; moreover, this model has been proven to be very effective in many coastal areas around the world [25–33]. The ADCIRC model is used for storm surge verification and inundation; the numerical simulation was based on the original continuous equation and the motion equation of the vertical average to calculate the variables, such as free surface undulation and two-dimensional flow velocity. In the equation of motion, the advection term, Coriolis force term, wind stress term, bottom friction term, lateral viscosity term, and tide are considered. In a spherical coordinate system, the continuous equation and the motion equation are expressed as follows:

$$\frac{\partial \zeta}{\partial t} + \frac{1}{R\cos\varphi}\frac{\partial UH}{\partial \lambda} + \frac{1}{R}\frac{\partial VH}{\partial \varphi} - \frac{VH\tan\varphi}{R} = 0 \tag{1}$$

$$\frac{\partial U}{\partial t} + \frac{U}{R\cos\varphi}\frac{\partial U}{\partial \lambda} + \frac{V}{R}\frac{\partial U}{\partial \varphi} - (\frac{U\tan\varphi}{R} + f)V = -\frac{1}{R\cos\varphi}\frac{\partial}{\partial \lambda}[\frac{p_s}{\rho_0} + g(\zeta - \eta)] + \frac{\tau_{s\lambda} - \tau_{b\lambda}}{\rho_0 H} + D_\lambda \tag{2}$$

$$\frac{\partial V}{\partial t} + \frac{U}{R\cos\varphi}\frac{\partial V}{\partial \lambda} + \frac{V}{R}\frac{\partial V}{\partial \varphi} + (\frac{U\tan\varphi}{R} + f)U = -\frac{1}{R}\frac{\partial}{\partial \varphi}[\frac{p_s}{\rho_0} + g(\zeta - \eta)] + \frac{\tau_{s\varphi} - \tau_{b\varphi}}{\rho_0 H} + D_\varphi \tag{3}$$

where λ, φ are the latitude and longitude, respectively, ς is the free surface height from sea level, U, V are the depth-averaged horizontal and vertical velocities, respectively, $H = \varsigma + h$ is the total depth, R is the radius of the Earth, $f = 2\Omega\sin\varphi$ and is the Coriolis parameter, Ω is the angular velocity of the Earth's rotation, g is the acceleration due to gravity, P_s is the atmospheric pressure, ρ_0 is the density of seawater, η is the tidal momentum for Newton, α is an effective resilience factor of the Earth, $\tau_{s\lambda}, \tau_{s\varphi}$ are the free surface stresses, $\tau_{b\lambda}, \tau_{b\varphi}$ are the bottom friction stresses, and D_λ, D_φ are the horizontal diffusion terms of the momentum equation.

The ADCIRC model uses the general wave continuity equation (GWCE) to replace the original continuity equation. The GWCE introduced a spatially variable numerical weighting parameter τ_0 to avoid problems using a Galerkin finite element spatial discretization

of the original from the equation; then, the momentum equation is substituted into the changed continuity equation. Compared with the original continuity equation, using the general wave continuity equation without convective acceleration can produce a damping effect on the short wave; thus, the calculation of the long wave becomes more convenient and accurate. At the same time, the GWCE equation is naturally decoupled, and the mass matrix is independent of time; thus, the solution of the model is relatively simple, which improves the computational efficiency and stability [24].

$$\begin{aligned}&\frac{\partial \zeta^2}{\partial t^2}+\tau_0\frac{\partial \zeta}{\partial t}+\frac{1}{R\cos\varphi}\frac{\partial}{\partial \lambda}\left\{\begin{array}{l}U\frac{\partial \zeta}{\partial t}-\frac{H}{R}\left(\frac{U}{\cos\varphi}\frac{\partial U}{\partial \lambda}+V\frac{\partial U}{\partial \varphi}\right)+\left(\frac{\tan\varphi}{R}U+f\right)VH-\\ \frac{H}{R\cos\varphi}\frac{\partial}{\partial \lambda}\left[\frac{P_s}{\rho_0}+g(\zeta-\alpha\eta)\right]+\frac{\tau_{s\lambda}}{\rho_0}-(\tau_*-\tau_0)UH+D_\lambda H\end{array}\right\}\\&+\frac{1}{R}\frac{\partial}{\partial \varphi}\left\{\begin{array}{l}V\frac{\partial \zeta}{\partial t}-\frac{H}{R}\left(\frac{U}{\cos\varphi}\frac{\partial V}{\partial \lambda}+V\frac{\partial V}{\partial \varphi}\right)-\left(\frac{\tan\varphi}{R}U+f\right)UH-\\ \frac{H}{R}\frac{\partial}{\partial \varphi}\left[\frac{P_s}{\rho_0}+g(\zeta-\alpha\eta)\right]+\frac{\tau_{s\varphi}}{\rho_0}-(\tau_*-\tau_0)VH+D_\varphi H\end{array}\right\}\\&-\frac{\tan\varphi}{R}\left(\frac{\partial VH}{\partial t}+\tau_0 VH\right)=0\end{aligned} \tag{4}$$

The main parameter settings of the model are listed in Table 1. The initial and boundary conditions of the model are provided in Table 2. Thus, these settings and conditions are used for model validation and numerical simulation.

Table 1. Model parameters settings.

Model Parameters	Setting Value	Description
NOLIBF	2	Parameter controlling the type of bottom stress parameterization
NOLIFA	2	Parameter controlling the finite amplitude terms
NTIP	1	Parameter controlling whether tidal potential and self-attraction/load tide forcings occur
NWS	8	Parameter controlling whether wind velocity or stress, wave radiation stress, and atmospheric pressure occur
τ_0	−3	Generalized wave continuity equation (GWCE)-weighting factor
DT	1	Model time step (in seconds)
A00, B00, C00	0.35, 0.30, 0.35	Time-weighting factors (at time levels $k+1$, k, and $k-1$, respectively) in the GWCE
ISOLVER	2	calculation method options

Table 2. Model boundary condition settings.

Model Boundary Condition	Setting Value	Description
The initial condition	$\zeta = u = v = 0$	At the beginning of model calculation, the sea level and velocity are zero
Open-boundary condition	Radiative boundary condition	Driven by eight constituents (M2, S2, K2, N2, K1, O1, P1, Q1), harmonic constants are taken from the global tidal model NAO99 [34], and these data are used to calculate the open-boundary tidal level with the tidal potential formula [24]
Land boundary condition	$V_n = 0$	The land boundary meets the non-incident condition, and the normal velocity is taken as zero

A wet-and-dry grid algorithm is used for the simulation of storm surge inundations. The minimum water depth Hmin is set to 0.05 m and serves as the critical value for the wet and dry grid states. When a dry point changes to a wet point and to ensure computational stability, the flow velocity U needs to be greater than the minimum velocity U_{min} (0.05 m/s) at the wet point. U is expressed as follows [24]:

$$U = \frac{g(\zeta_{i-1}-\zeta_i)}{\tau_{bi}\Delta x_i} \tag{5}$$

where ζ_{i-1} and ζ_i are the tide levels of the current and adjacent grids, respectively, τ_{bi} is the bottom friction of the current grid, and Δx_i is the distance between the current and adjacent grids. The position and height of the seawall are set in the model grid. When the tide level of the seawall grid exceeds the height of the seawall at a certain time, overflow occurs. The expression of the seawater overflow rate Q per unit length is as follows [24]:

$$Q = C_d \frac{2}{3} \sqrt{2gh_1}^{3/2} \tag{6}$$

where Q is the seawater overflow, h_1 is the height of seawater overflowing the seawall, and C_d is the flow coefficient, which is expressed as follows [24]:

$$C_d = 0.611 * [(1 + \frac{{v_1}^2}{2gh_1})^{3/2} - (\frac{{v_1}^2}{2gh_1})^{3/2}] \tag{7}$$

where v_1 is the seawater flow velocity corresponding to the height of the seawall.

2.2. Data Sources

The data required for the storm surge inundation simulation include typhoon, tide level, water depth, digital elevation model (DEM) elevation, and seawall data. The sources and descriptions of these data are provided in Table 3.

Table 3. Data sources used in the model.

Data	Source	Description
Typhoon data	China Meteorological Administration (CMA) [35,36]	These data are collected at six-hour intervals and include information on the impact time, location, minimum air pressure at the typhoon center, and maximum wind speed of the typhoon.
Tide level data	National Marine Data Center of China [37]	Hourly tide level data from the Sanzao tide gauge station in Guangdong Province were used.
Water depth data	National Marine Environment Forecasting Center of China [38] National Catalogue Service for Geographic Information of China [39]	These data for the open sea have a spatial resolution of 2′. These data for sea area near the study area have a spatial resolution of 25 m and were collected in 2022.
Geographic information data	National Catalogue Service for Geographic Information of China [39]	The DEM data have a spatial resolution of 10 m and were collected in 2021. The seawall data have a spatial resolution of 50 m and were collected in 2022.

Typhoon data: The *Typhoon Yearbook* data from the China Meteorological Administration (CMA) were used [35,36]. These data were used to construct wind fields to drive the storm surge model.

Tide level data: Tide level data from the Sanzao tide gauge station in Guangdong Province were used [37].

Water depth data: The water depth data included two parts: (1) the water depth data used by the operational storm surge forecast system of the National Marine Environment Forecasting Center of China [38], with a spatial resolution of 2′, were used for the open sea; (2) the survey data from the sea area near the study area (Figure 1a), with a spatial resolution of 25 m and observed in 2022.

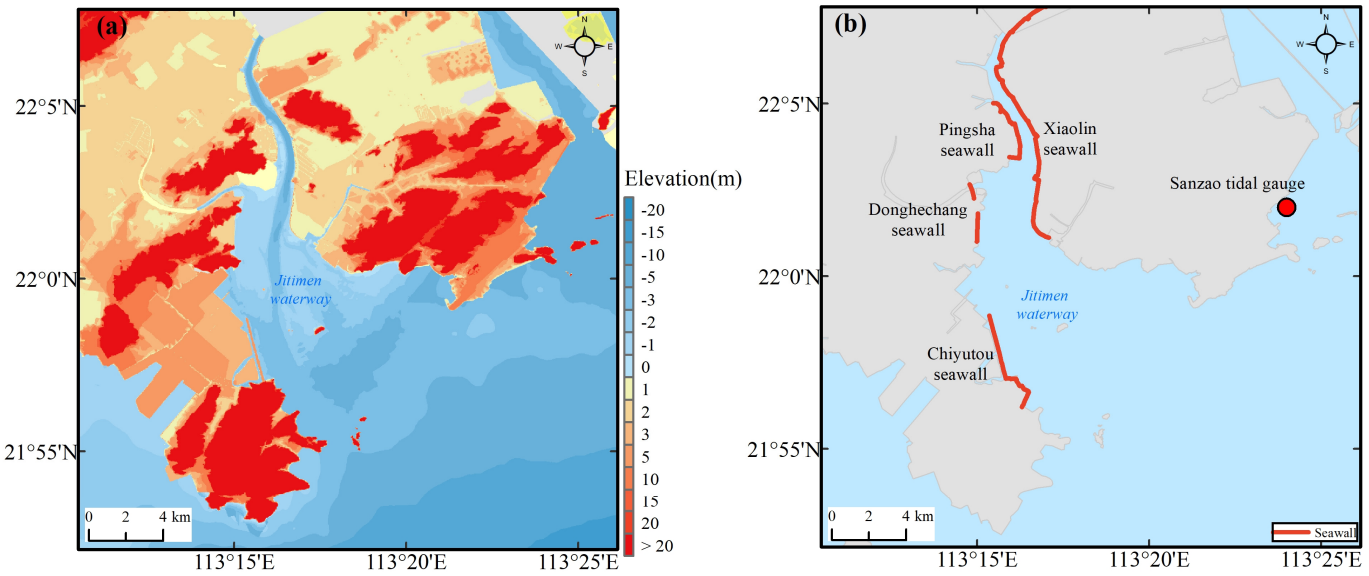


Figure 1. Distributions of the topography (**a**) and seawall (**b**) in the study area.

Geographic information data: These data include digital elevation model (DEM) data and coastal seawall data covering the study area. The DEM data (2021) have a spatial resolution of 10 m (Figure 1a), and the seawall data (2022) have a spatial resolution of 50 m. These data were collected mainly on both sides of the Jitimen estuary and east of the Gaolan Port, including the Xiaolin, East Pingsha, Donghechang, and Chiyutou seawalls (Figure 1b), with elevations in the range of 2.6 to 4.2 m (Pearl River datum; the same below).

2.3. Storm Surge Simulation Validation

The storm surge model uses an unstructured triangular grid to describe complex nearshore terrain. The calculation region includes most of the South China Sea, with an open-boundary grid resolution of 20 km. The grid is refined in the study area. The land grid has a resolution of 30–40 m, and the Jitimen channel grid has a resolution of 50–100 m. The entire set of grids consists of 345,926 grid cells and 177,053 grid points, with approximately 70% of the grid cells distributed on the land and in the channels of the study area. An 8 m land contour is used as the land boundary. Figure 2 shows the grid distribution in the overall study area and in the key regions.

The Jitimen area belongs to Zhuhai City, Guangdong Province, China, and is located on the west side of the Pearl River Estuary. Storm surges are frequent and severe disasters occur in this area. According to the statistics of the storm surge disasters from 1949 to 2022, there is an average of one significant or severe storm surge every 2 to 3 years, and the number of storm surge disasters has shown a sharp increasingly trend in the past decade. The No. 13 super typhoon Hato in 2017 and the No. 22 super typhoon Mangkhut in 2018 were considered severe storm surge disasters and are selected as case examples for the model validation. Hindcast validation is conducted using tidal data from the Sanzao tide gauge station (location shown in Figure 1b).

Figure 3 shows a comparison of the simulated hindcasts and actual measurements for storm surges caused by the Hato and Mangkhut typhoons at the Sanzao tide gauge station. The hourly curves show that the simulated hindcasts closely match the actual measurements. The simulated and measured maximum storm surge errors are 3.2% and 5.0%, respectively, and the simulated and measured highest tide level errors are 1.2% and 2.4%, respectively. These results indicate that the model can effectively represent the storm surge and tide level changes caused by strong typhoons and, hence, can be used for the subsequent numerical experiment on storm surge inundation.

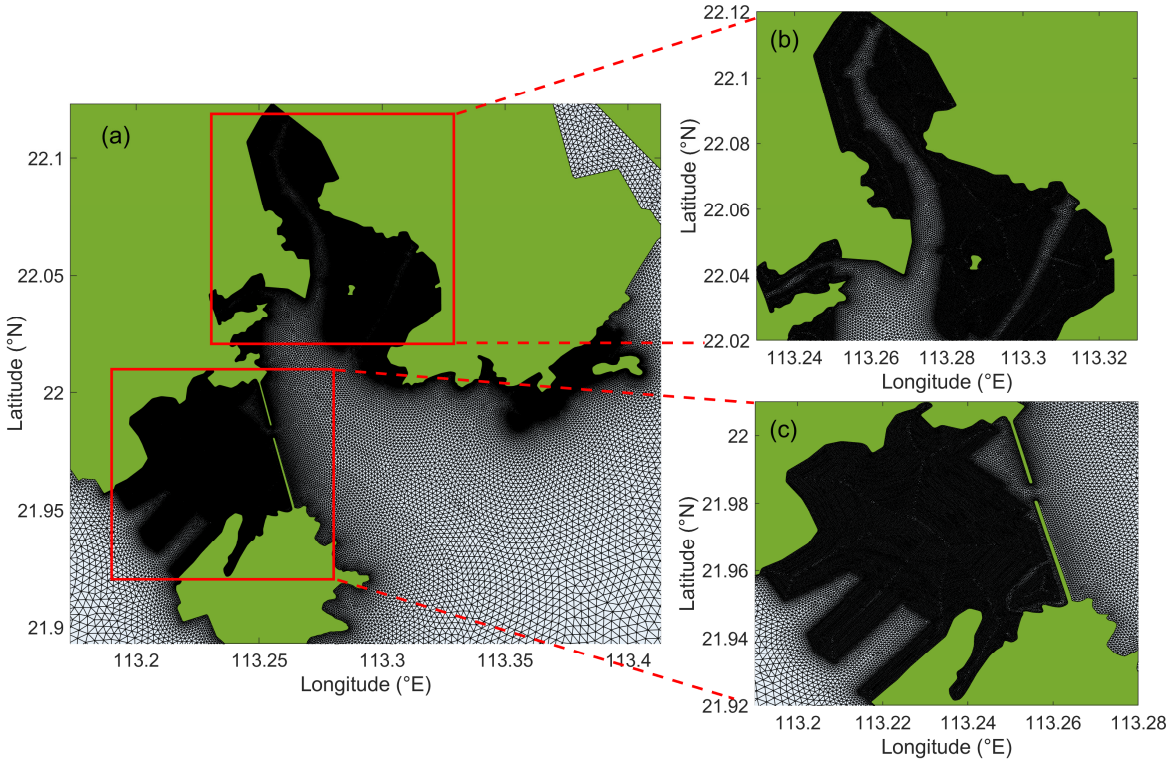


Figure 2. Grid distribution in the study area (**a**), grids on the sides of the Jitimen waterway (**b**) and grids of the Gaolan Port (**c**).

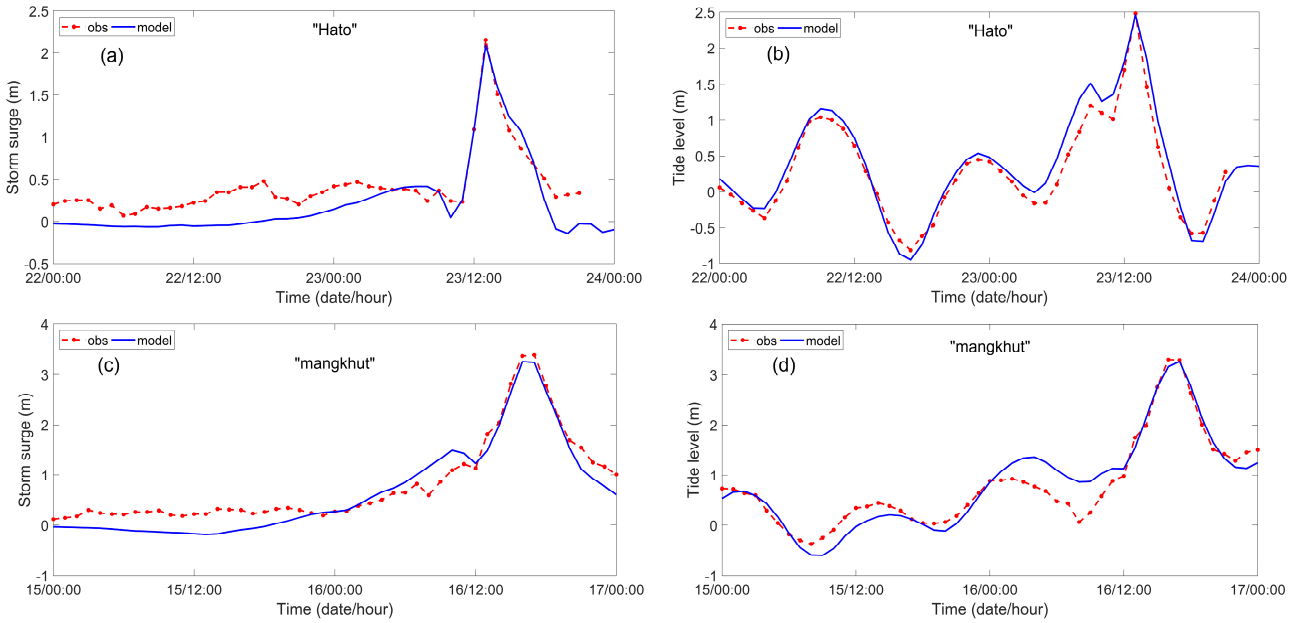


Figure 3. Comparison of the measurements and simulated hindcasts for the Sanzao tide gauge station: Storm surge of Hato (**a**), total tide level of Hato (**b**), storm surge of Mangkhut (**c**), and total tide level of Mangkhut (**d**).

3. Results

To carry out research on storm surge inundations in small regions, it is necessary to conduct statistical analyses of historical storm surge data, disaster data, and typhoon information of the study area, and their results can be used as oceanographic and meteorological background parameters. In addition, the factors affecting storm surge inundations include

typhoon landfall intensity, landfall location, landfall direction, typhoon speed, astronomical tides, nearshore waves, and nearshore topography. Therefore, reasonable experiments need to be set up, and the simulation results need to be analyzed.

3.1. Statistics of Historical Typhoons and Storm Surges

In terms of typhoon landfall intensity, from 1949 to 2022, there were 209 typhoons passing within 300 km of the study area, an average of approximately 2.9 typhoons per year [35,36]. The typhoons that caused the top ten historical tide levels at the Sanzao tide gauge station were typhoons 8908, 9302, 9316, 9615, 0307, 0814, 0915, 1415, 1713, and 1822. Among them, there were four at the typhoon level, five at the strong typhoon level, and one at the super typhoon level. The typhoons that caused the top two historical tide levels in the study area were typhoons 1822 and 0814; both of these had strong landfall intensities. Evidently, when the maximum wind speed in the typhoon center is greater than 35 m/s, storm surge disasters are likely to occur in the study area.

In terms of typhoon landfall, between 1949 and 2022, there were 183 typhoons that passed and made landfall within 300 km of the study area [35,36], accounting for 87.6% of the total typhoons. In terms of the typhoon landfall direction, the primary direction was in the northwest quadrant (W, WNW, NW, NNW, and N), accounting for 84.7% of all landfall typhoons, and the typhoons that caused the top ten historical tide levels in the study area were all in this direction (Figure 4). In terms of typhoon speed, approximately 52.8% of the typhoons had a speed ranging from 15 to 25 km/h, with an average speed of 19.8 km/h. In terms of typhoon impact time, typhoons influence the study area from April to December each year, with summer (July to September) being the predominant period of influence, accounting for 67.9% of all typhoons.

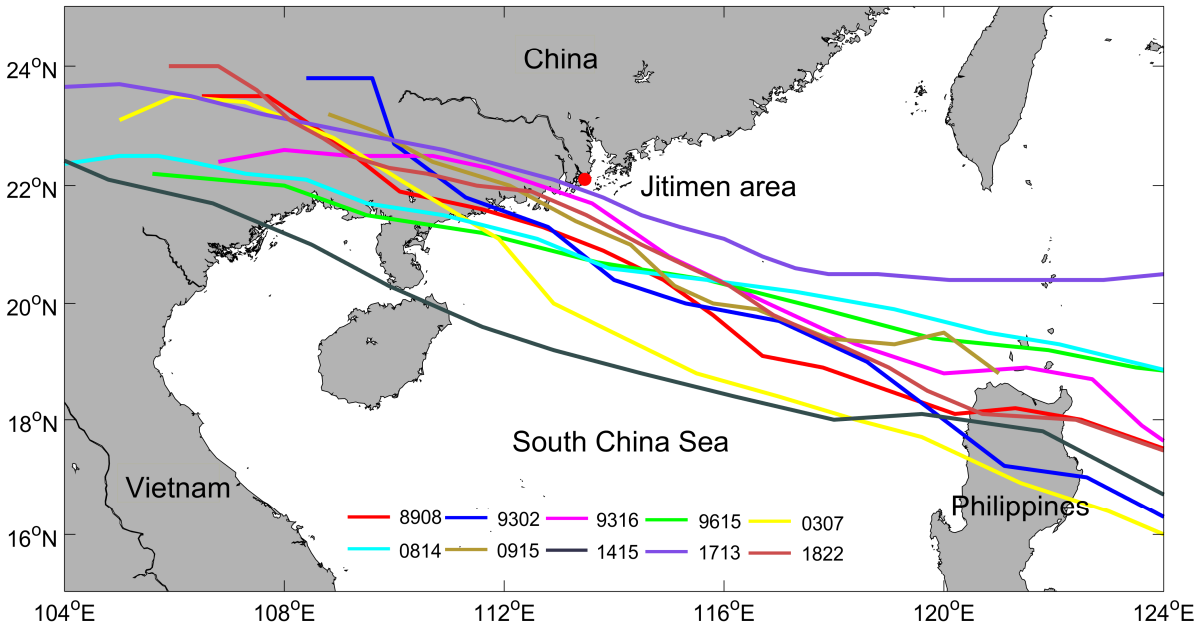


Figure 4. Paths of the typhoons that caused the top ten historical tide levels at the Sanzao tide gauge.

3.2. Settings for the Numerical Simulations of the Multifactor Storm Surge Inundation

According to the historical storm surge data, forecast experience, and topographic features, the typhoon landfall intensity, landfall direction, landfall location, and astronomical tide are the main factors influencing storm surge inundations, and the measured tide levels at coastal tide gauge stations are an important basis for recording storm surge events. Regardless of the combination of and changes in influencing factors, the measured tide levels at the tide gauge stations can likely be used to determine the storm surge inundation state. This deduction needs to be verified in the subsequent research to this study. Based

on the above historical typhoon statistics, we set the typhoon speed to 20 km/h and superimposed the astronomical tide curve from the average value of astronomical high tides for July to September at the Sanzao tide gauge station to establish three experimental schemes of the factors influencing storm surge inundation as follows:

Scheme A: Storm surge inundation simulation with different landfall locations.

The typhoon moves in the west-northwest (WNW) direction with a landfall intensity of 930 hPa. Three landfall location scenarios are set up such that the total tide levels at the Sanzao tide gauge station are similar to each other to assess the differences in storm surge inundation (see Figure 5a for the typhoon paths).

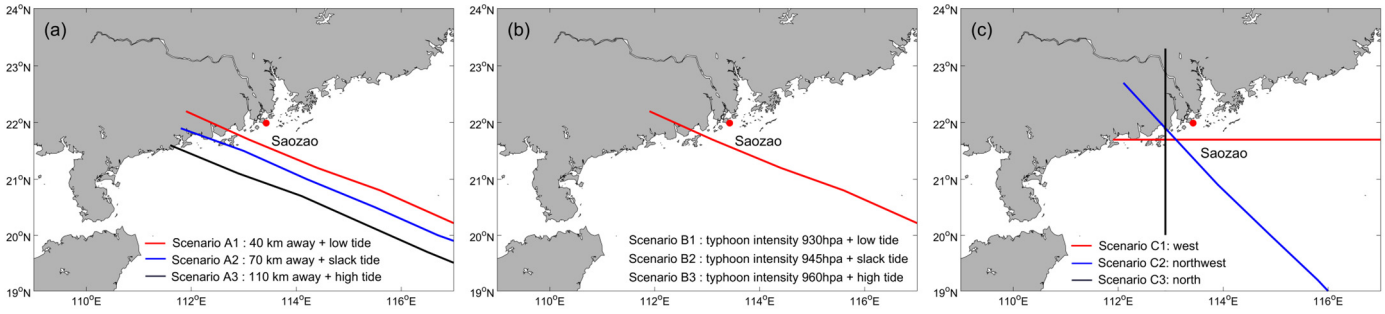


Figure 5. Typhoon path settings for the simulation schemes with the three influencing factors: (**a**) landfall location, (**b**) landfall intensity, and (**c**) landfall direction.

Scenario A1: The typhoon passes at a distance of 40 km from the south of the study area, and the maximum storm surge is superimposed on the astronomical low tide;

Scenario A2: The typhoon passes at a distance of 70 km from the south of the study area, and the maximum storm surge is superimposed on the astronomical slack tide;

Scenario A3: The typhoon passes at a distance of 110 km from the south of the study area, and the maximum storm surge is superimposed on the astronomical high tide.

Scheme B: Storm surge inundation simulation with different landfall intensities.

The typhoon moves in the west-northwest (WNW) direction and passes 40 km south of the study area. Three typhoon intensity scenarios are set up such that the total tide levels at the Sanzao tide gauge station are similar to each other to assess the differences in storm surge inundation (see Figure 5b for the typhoon paths).

Scenario B1: The landfall intensity is 930 hPa, and the maximum storm surge is superimposed on the astronomical low tide;

Scenario B2: The landfall intensity is 945 hPa, and the maximum storm surge is superimposed on the astronomical slack tide;

Scenario B3: The landfall intensity is 960 hPa, and the maximum storm surge is superimposed on the astronomical high tide.

Scheme C: Storm surge inundation simulation with different landfall directions.

The typhoon intensity is 945 hPa. Three typhoon landfall direction (west, northwest, and north) scenarios are set up such that the total tide levels at the Sanzao tide gauge station are similar to each other to assess the differences in storm surge inundation (see typhoon tracks in Figure 5c).

Scenario C1: The landfall direction is westward;

Scenario C2: The landfall direction is northwest;

Scenario C3: The landfall direction is northward.

3.3. Multifactor Numerical Simulation Analysis of Storm Surge Inundation

Based on the above experimental settings, the storm surge inundation model is driven by the wind field of the Holland typhoon model [40]. Figure 6 and Table 4 show the diagrams and statistics, respectively, of the storm surge inundation area and depth under Scenarios A1, A2, and A3. When the typhoon landfall intensity and direction remain unchanged, the landfall location is variable, and the highest tide levels at the Sanzao tide

gauge station are similar, based on the distribution of the maximum storm surge inundation field (Figure 6). With the exception of a small difference in the inundation range in the eastern part of the Jitimen estuary, the inundation ranges and depths are similar among the three scenarios. From the difference statistics (Table 4) under the three scenarios, there is an approximately 5% difference in the inundation area and a less than 5% difference in the average inundation depth; these results indicate minimal variations.

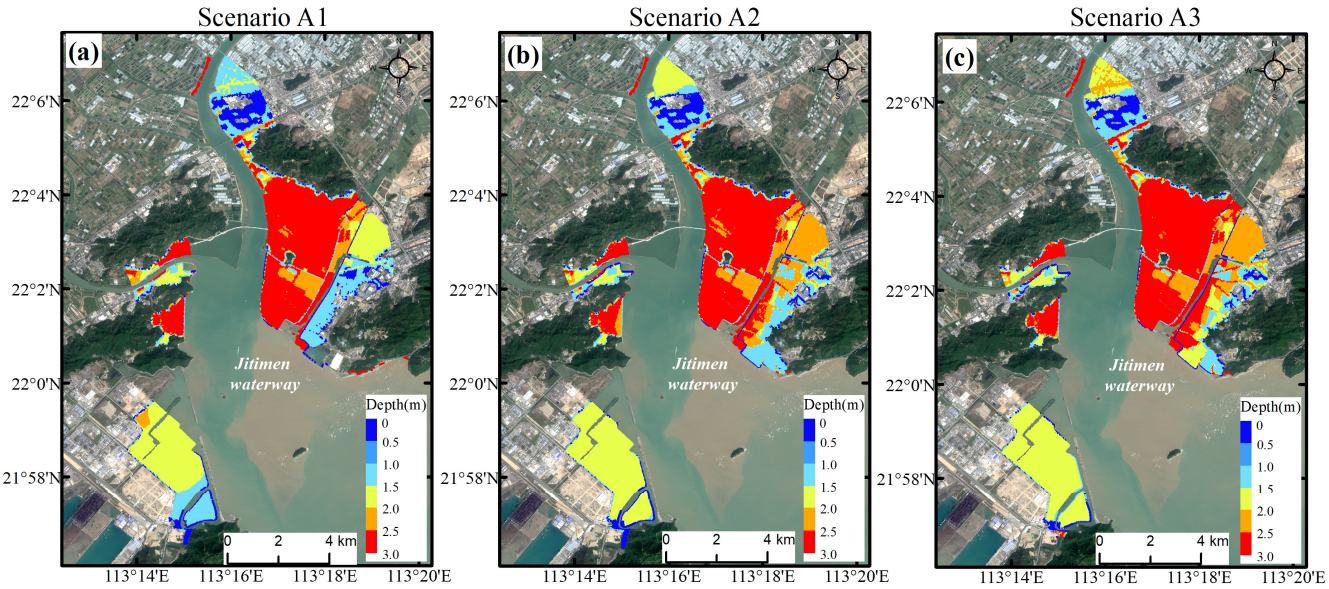


Figure 6. Comparison of the storm surge inundation areas and depths under the three scenarios of the typhoon landfall location scheme: scenario A1 (**a**), scenario A2 (**b**), and scenario A3 (**c**).

Table 4. Statistics on the storm surge inundation areas and depths under the three scenarios of the typhoon landfall location scheme.

Simulation Scenario	Highest Tide Level at the Sanzao Station (m)	Duration Exceeds 3 m at the Sanzao Station (hr)	Inundation Area (km^2)	Difference from A1	Average Inundation Depth (m)	Difference from A1
A1	3.57	3.13	35.16	0	1.99	0
A2	3.58	3.25	36.51	3.8%	2.03	2.0%
A3	3.60	3.34	37.12	5.6%	2.08	4.5%

Figure 7 and Table 5 show the images and statistics of the storm surge inundation areas and depths under scenarios B1, B2, and B3, respectively. When the typhoon landfall location and direction remain unchanged, the landfall intensity varies, and the highest tide levels at the Sanzao tide gauge station are similar, according to the distribution of the maximum storm surge inundation field (Figure 7); with the exception of a very minor difference in the inundation range in the eastern part of the Jitimen estuary, the inundation areas and depths are very similar under the three scenarios. As for the difference statistics (Table 5), under the three scenarios, the difference in the inundation area is less than 5%, and the difference in the average inundation depth is less than 5%, indicating minimal variations.

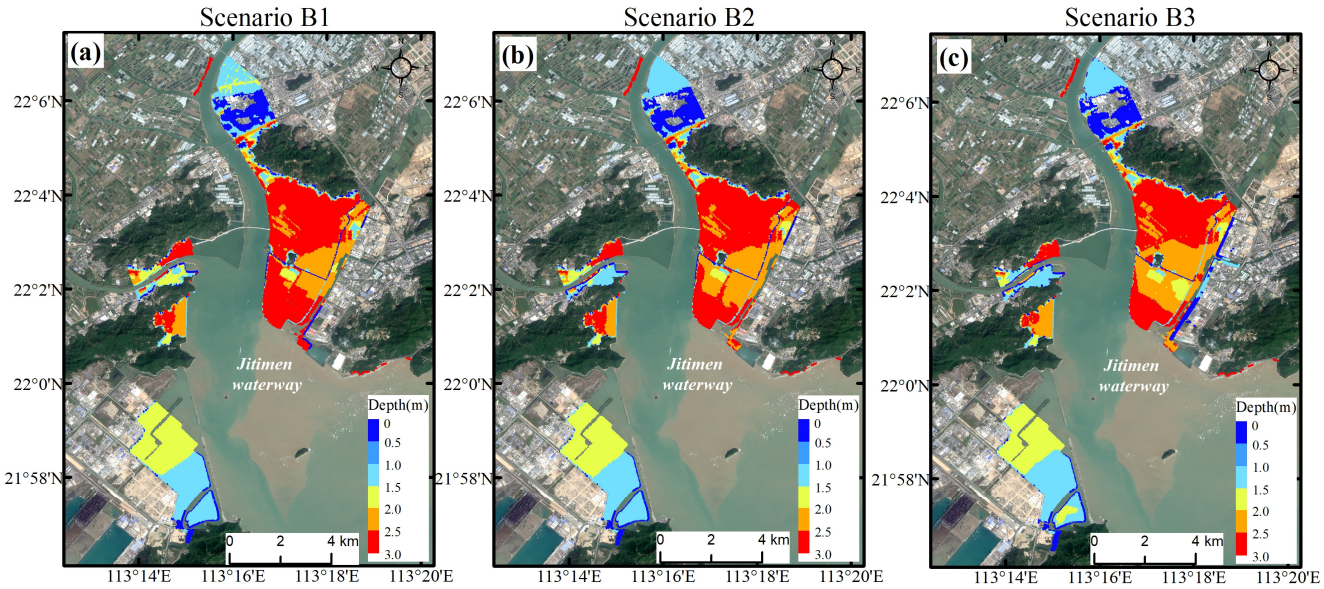


Figure 7. Comparison of the storm surge inundation areas and depths under the three scenarios of the typhoon landfall intensity scheme: scenario B1 (**a**), scenario B2 (**b**), and scenario B3 (**c**).

Table 5. Statistics of the storm surge inundation areas and depths under the three scenarios of the typhoon landfall intensity scheme.

Simulation Scenario	Highest Tide Level at the Sanzao Station (m)	Duration Exceeds 3 m at the Sanzao Station (hr)	Inundation Area (km^2)	Difference from B1	Average Inundation Depth (m)	Difference from B1
B1	3.44	2.79	29.13	0	1.96	0
B2	3.46	2.88	29.01	0.4%	1.93	1.5%
B3	3.47	3.00	30.47	4.7%	1.88	4.1%

Figure 8 and Table 6, respectively, show the images and statistics of the storm surge inundation areas and depths under scenarios C1, C2, and C3. When the typhoon landfall location and intensity remain unchanged, the landfall direction is variable, and the highest tide levels at the Sanzao tide gauge station are similar, based on the distribution of the maximum storm surge inundation field (Figure 8). However, notable differences are observed in the inundation areas and depths under the three scenarios. The inundation extent of the land area to the east of the Jitimen estuary widely varies, with the largest inundation area and average inundation depth occurring under scenario C3, followed by those under scenario C2, and the smallest under scenario C1. According to the difference statistics (Table 6), the inundation areas under scenarios C2 and C3 are 16.8% and 29.8% larger than that under scenario C1, respectively, and the average inundation depths under scenarios C2 and C3 are 5.8% and 14.7% larger than that under scenario C1, respectively.

Table 6. Statistics of the storm surge inundation areas and depths under the three scenarios of the typhoon landfall direction scheme.

Simulation Scenario	Highest Tide Level at the Sanzao Station (m)	Duration Exceeds 3 m at the Sanzao Station (hr)	Inundation Area (km^2)	Difference from C1	Average Inundation Depth (m)	Difference from C1
C1	3.51	2.83	30.84	0	1.91	0
C2	3.52	3.24	36.03	16.8%	2.02	5.8%
C3	3.54	3.71	40.02	29.8%	2.19	14.7%

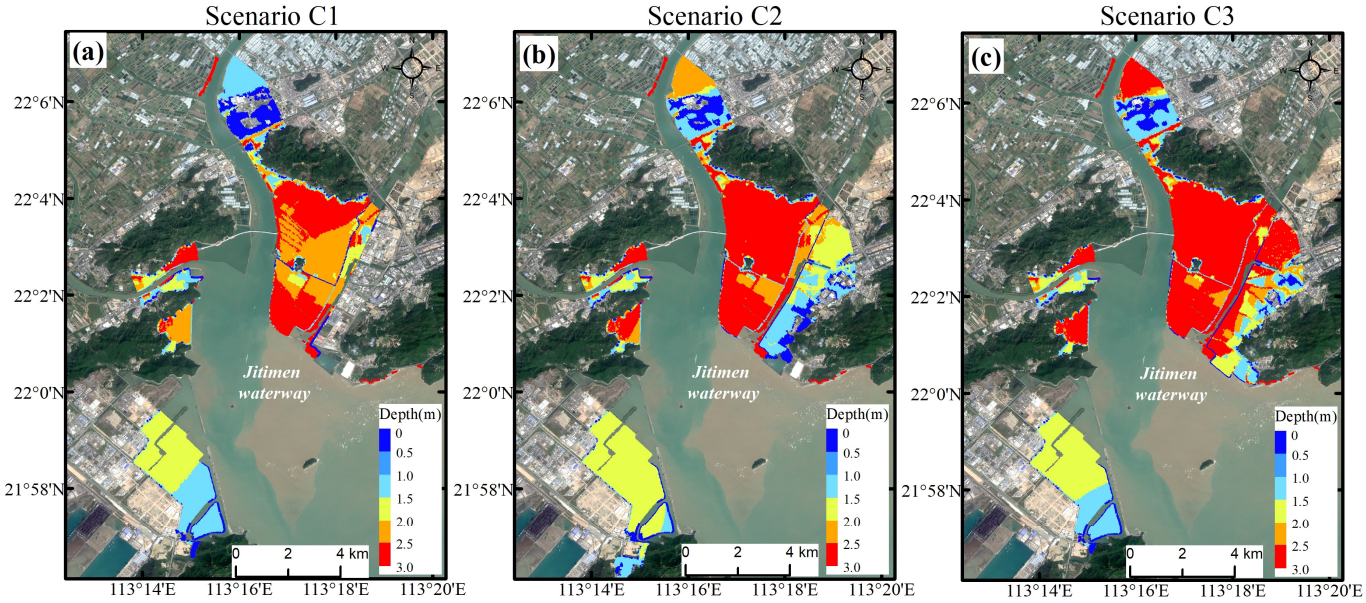


Figure 8. Comparison of the storm surge inundation areas and depths under the three scenarios of the typhoon landfall direction scheme: scenario C1 (**a**), scenario C2 (**b**), and scenario C3 (**c**).

The above numerical experiments indicate that the study area has been flooded when the tide level exceeds 3 m at the Sanzao station. Based on Tables 4–6, the differences in storm surge inundation among the three scenarios are analyzed in terms of the duration of high tide levels (exceeding 3 m) at the Sanzao station. In scenarios A1, A2, and A3, the durations of high tide levels exceeding 3 m are 3.13, 3.25, and 3.34 h, respectively, with differences of less than 7%. In scenarios B1, B2, and B3, the durations of the high tide levels are 2.79, 2.88, and 3.00 h, respectively, with differences of less than 8%. Evidently, under conditions where the highest tide levels at the Sanzao station and the duration of high tide levels are similar, the differences in the storm surge inundation area and average inundation depth among the three scenarios for typhoon landfall locations (A1, A2, and A3) are very small. Similarly, the differences in storm surge inundation area and average inundation depth among the three scenarios for typhoon landfall intensities (B1, B2, and B3) are also very small. However, in scenarios C1, C2, and C3, the durations of high tide levels exceeding 3 m are 2.83, 3.24, and 3.71 h, respectively. C2 and C3 are 13.1% and 31.1% larger than C1, respectively, showing significant differences. This difference is attributed to the topographic features and the direction of the typhoon landfall.

The Jitimen waterway is a north–south trumpet-shaped estuary, with the mouth facing south. When the typhoon landfall location and intensity remain unchanged and the landfall direction is westward (scenario C1), the study area is mainly affected by easterly winds. The Jitimen estuary is not conducive to the accumulation of storm surges, with a high tide duration of 2.83 h; this duration is the shortest among the three scenarios. When the typhoon landfall direction is northwestward (scenario C2), the study area is mainly affected by southeasterly winds. Compared to that in scenario C1, the Jitimen estuary is more conducive to the accumulation of storm surges, with a high tide duration of 3.24 h; this duration is 13.1% longer than that in scenario C1. When the typhoon landfall direction is northward (scenario C3), the study area is mainly affected by southerly winds; compared to those in scenarios C1 and C2, C3 is most conducive to the accumulation of storm surges, with a high tide duration of 3.71 h; this duration is 33.1% longer than that in scenario C1. In the typhoon landfall direction scheme, a longer high tide duration results in a greater total amount of seawater entering the Jitimen estuary area during the storm surge, leading to a larger inundation area and a correspondingly greater average inundation depth.

4. Discussion and Conclusions

With global climate change, the risk of extreme storms and the resulting storm surges in estuarine areas is increasing. Our numerous research findings indicate that the factors influencing storm surges in estuarine areas are diverse and complex, involving multiple aspects. Storm surges can interact with fragile estuarine ecosystems, river runoff, and seawalls [18,20,22] and can also affect the hydrodynamics and geomorphic features of estuaries [19]. Research in this field is extensive and beneficial. The factors influencing storm surges in estuarine areas can be divided into two categories: (1) different hydrodynamic influencing factors in estuaries, such as tides, runoff, waves, nearshore structures, and ecosystems, and (2) different meteorological influencing factors, mainly involving typhoon landfall intensity, location, and direction. Scholars have conducted extensive research on the first category of influencing factors and have achieved abundant research results; however, research on storm surge inundation under different meteorological influencing factors is very limited. Research in the latter area has the potential to improve the forecast level of storm surge inundation. The circulation range of typhoons is generally hundreds of kilometers or even larger, while the range of small-scale estuaries is generally less than 200 km. The circulation range of typhoons is much larger than that of small-scale estuaries, and the influencing factors of typhoons can alter the characteristics of storm surges in small-scale estuarine areas. From the perspective of defending against storm surge disasters in estuarine areas, accurate storm surge forecasts are needed before disasters occur, reasonable storm surge decision-making information is needed when disasters occur, and detailed storm surge investigations and assessments are needed after disasters occur. Clearly, forecasting and researching storm surge inundation in estuarine areas are extremely important tasks.

With the advancement of computer technology and the development of storm surge models, numerical forecasting models for storm surges provide favorable support for predicting storm surge inundation in estuarine areas. Storm surge models require high-resolution computational grids (in the order of meters or tens of meters) to characterize the complex terrain of estuarine areas. The computation of a storm surge inundation event takes a long time (from tens of minutes to several hours); thus, storm surge decision-making is negatively affected due to the time-consuming computations with numerical forecasting models. Additionally, typhoon forecast information is updated every few hours, posing a challenge for storm surge inundation model calculations. In contrast to numerical forecasting systems, a multi-scenario storm surge inundation database constructed based on historical typhoon information can be used for storm surge inundation forecasting; this is a method closely related to the present study. Before the typhoon's impact, inputting the typhoon forecast information and forecasted tide levels for estuarine areas into the database can yield inundation forecasting results within minutes, facilitating the dissemination of storm surge warnings and decision-making information; this method is quicker than numerical forecasting models. However, this method is only applicable to small-scale estuarine areas, and the storm surge inundation databases for each estuarine area may differ, requiring continuous research support.

In this paper, using the Jitimen area as a study area, we established and validated a numerical model for storm surge inundation with refined grids in small regions, conducted a multifactor, multi-scenario numerical simulation of storm surge inundation based on the statistical characteristics of historical data affecting the meteorology and occurrence of storm surges in the study area, analyzed the differences in the numerical results, and summarized the significant factors influencing storm surge inundation. The main conclusions of this paper are as follows:

(1) High-resolution basic geographic information data for the study area were obtained, and a numerical model for storm surge inundation based on unstructured triangular grids was established, with a refined grid resolution of 30–40 m for the land region. The 2017 super typhoon Hato and the 2018 super typhoon Mangkhut were selected as validation case examples. The errors between simulated and measured maximum storm surges were 3.2% and 5.0%, respectively, and the errors between simulated

and measured highest tide levels were 1.2% and 2.4%, respectively, at the Sanzao tide gauge station, indicating excellent model performance.

(2) Based on the typhoon data from 1949 to 2022 and historical data from the Sanzao tide gauge station in the study area, the main characteristics of the typhoons affecting the study area were calculated. It was found that the typhoon intensity must reach at least the typhoon level for storm surge disasters to occur, the main typhoon landfall direction was found to occur in the northwest quadrant (W, WNW, NW, NNW, and N), the average typhoon speed was approximately 20 km/h, and the main impact occurred during the summer months (July to September) each year.

(3) Based on the statistical data of historical typhoons, using a typhoon speed of 20 km/h, and superimposing the average value of astronomical high tides in July to September, three experimental schemes with different typhoon landfall locations, intensities, and directions that influence storm surge inundation were set up to assess the differences in the numerical results. The results showed that when the typhoon landfall direction remained unchanged and the highest tide levels at the Sanzao tide gauge station were similar, the differences between the numerical results for the typhoon landfall location and typhoon intensity schemes were less than 5%, and the inundation characteristics were similar. However, when the typhoon location and intensity were unchanged and the highest tide levels at the Sanzao tide gauge station were similar, the numerical results for the typhoon landfall direction scheme differed significantly. The inundation areas under the north and northwest direction scenarios were 16.8% and 29.8% larger than those under the west direction scenario, respectively, and the average inundation depths under the north and northwest direction scenarios were 5.8% and 14.7% greater than those under the west direction scenario, respectively, indicating large differences in inundation characteristics.

The reasons for the differences in the storm surge inundation among the three scenarios were analyzed using the duration of the high tide levels (exceeding 3 m) at the Sanzao tide gauge station. Under the conditions with relatively small differences in the maximum tide levels and the high tide duration at the Sanzao station, the differences in the storm surge inundation area and average inundation depth among the three scenarios of typhoon landfall location (A1, A2, and A3) and the three scenarios of typhoon landfall intensity (B1, B2, and B3) are minimal. However, a significant difference in the duration of the high tide levels occurs among the three scenarios of the typhoon landfall direction (C1, C2, and C3), and differences in the storm surge inundation characteristics among them are also evident. The numerical results revealed that when the highest tide levels are similar, compared with the intensity and location of the typhoon, the typhoon landfall direction and the topographic characteristics of the estuary have a greater impact on storm surge inundation.

Author Contributions: Conceptualization, C.F. and S.L.; methodology, C.F. and S.L.; software, Q.L. and H.C.; validation, Q.L.; formal analysis, Q.L. and S.L.; investigation, Y.G. and H.C.; resources, Y.G.; writing—original draft preparation, C.F.; writing—review and editing, C.F. and S.L.; visualization, Y.G. All authors have read and agreed to the published version of the manuscript.

Funding: This research was funded by the Natural Science Foundation of China (No. 42394134 and No. 42076214).

Institutional Review Board Statement: Not applicable.

Informed Consent Statement: Not applicable.

Data Availability Statement: The data are available upon request from the corresponding author.

Acknowledgments: The authors would like to thank the reviewers who made constructive suggestions throughout the review process.

Conflicts of Interest: The authors declare no conflicts of interest.

References

1. Yu, F.J.; Dong, J.X.; Ye, L.; Hou, J.; Li, M.; Liu, S.; Wu, S.; Liu, Q.; Fu, X.; Fu, C. *Collection of Storm Surge Disasters Historical Data in China 1949–2009*; China Ocean Press: Beijing, China, 2015. (In Chinese)
2. Li, L.; Yang, J.; Lin, C.-Y.; Chua, C.T.; Wang, Y.; Zhao, K.; Wu, Y.-T.; Liu, P.L.-F.; Switzer, A.D.; Mok, K.M.; et al. Field Survey of Typhoon Hato (2017) and a Comparison with Storm Surge Modeling in Macau. *Nat. Hazards Earth Syst. Sci.* **2018**, *18*, 3167–3178. [CrossRef]
3. Yang, J.; Li, L.; Zhao, K.; Wang, P.; Wang, D.; Sou, I.M.; Yang, Z.; Hu, J.; Tang, X.; Mok, K.M.; et al. A comparative study of Typhoon Hato (2017) and Typhoon Mangkhut (2018)—Their impacts on coastal inundation in Macau. *J. Geophys. Res. Ocean.* **2019**, *124*, 9590–9619. [CrossRef]
4. Kemp, A.C.; Horton, B.P.; Donnelly, J.P.; Mann, M.E.; Vermeer, M.; Rahmstorf, S. Climate related sea-level variations over the past two millennia. *Proc. Natl. Acad. Sci. USA* **2011**, *108*, 11017–11022. [CrossRef]
5. Kopp, R.E.; Kemp, A.C.; Bittermann, K.; Horton, B.P.; Donnelly, J.P.; Gehrels, W.R.; Hay, C.C.; Mitrovica, J.X.; Morrow, E.D.; Rahmstorf, S. Temperature-driven global sea-level variability in the Common Era. *Proc. Natl. Acad. Sci. USA* **2016**, *113*, 1434–1441. [CrossRef]
6. Parker, A. Sea level trends at locations of the United States with more than 100 years of recording. *Nat. Hazards* **2013**, *65*, 1011–1021. [CrossRef]
7. Wang, H.; Liu, Q.; Li, H.; Li, W.; Jin, B. Latest research and progress on sea level change. *Mar. Inf.* **2018**, *33*, 19–25, 54. (In Chinese)
8. Shan, K.; Lin, Y.; Chu, P.-S.; Yu, X.; Song, F. Seasonal advance of intense tropical cyclones in a warming climate. *Nature* **2023**, *623*, 83–89. [CrossRef]
9. Garner, A.J.; Mann, M.E.; Emanuel, K.A.; Kopp, R.E.; Lin, N.; Alley, R.B.; Horton, B.P.; DeConto, R.M.; Donnelly, J.P.; Pollard, D. Impact of climate change on New York City's coastal flood hazard: Increasing flood heights from the preindustrial to 2300 CE. *Proc. Nat. Acad. Sci. USA* **2017**, *114*, 11861–11866. [CrossRef]
10. Fu, X.; Hou, J.; Liu, Q.; Li, M.; Liang, S. Evaluation of surge hazard based on a storm surge hazard indicator along the mainland coast of China. *Nat. Hazards* **2023**, *116*, 3481–3493. [CrossRef]
11. Kerr, P.C.; Martyr, R.C.; Donahue, A.S.; Hope, M.E.; Westerink, J.J.; Luettich, R.A.; Kennedy, A.B.; Dietrich, J.C.; Dawson, C.; Westerink, H.J. U.S. IOOS coastal and ocean modeling testbed: Evaluation of tide, wave, and hurricane surge response sensitivities to mesh resolution and friction in the Gulf of Mexico. *J. Geophys. Res. Ocean.* **2013**, *118*, 4633–4661. [CrossRef]
12. Li, T.; Fu, C.; Wang, F.; Dong, J. Storm surge disaster risk assessment and zoning, taking Cangnan County for instance. *Procedia IUTAM* **2017**, *25*, 92–99. [CrossRef]
13. Sahoo, B.; Bhaskaran, P.K. Prediction of storm surge and coastal inundation using Artificial Neural Network—A case study for 1999 Odisha Super Cyclone. *Weather Clim. Extrem.* **2019**, *23*, 100196. [CrossRef]
14. Zhang, M.; Luo, J.; Hu, J.L.; Zeng, X. Inundation risk assessment of storm surge along Lei Zhou coastal areas. *J. Trop. Oceanogr.* **2019**, *38*, 1–12. (In Chinese)
15. Hou, Y.J.; Yin, B.S.; Guan, C.L.; Guo, M.; Liu, G.; Hu, P. Progress and Prospect in Research on Marine Dynamic Disasters in China. *Oceanol. Limnol. Sin.* **2020**, *51*, 759–767. (In Chinese) [CrossRef]
16. Wang, K.; Hou, Y.; Li, S.; Du, M.; Li, R. Numerical study of storm surge inundation in the southwestern Hangzhou Bay region during typhoon Chan-Hom in 2015. *J. Ocean. Univ. China* **2020**, *19*, 263–271. [CrossRef]
17. Zhang, L.; Fu, C.F.; Dong, J.X.; Yu, F. Numerical simulation of storm surge inundation in block scale. *Haiyang Xuebao* **2021**, *43*, 38–49. (In Chinese)
18. Silveira, F.; Lopes, C.L.; Pinheiro, J.P.; Pereira, H.; Dias, J.M. Coastal Floods Induced by Mean Sea Level Rise—Ecological and Socioeconomic Impacts on a Mesotidal Lagoon. *J. Mar. Sci. Eng.* **2021**, *9*, 1430. [CrossRef]
19. Kristian, K.; Rafael, C.; Colin, W. Modelling Hydrodynamic Impacts of Sea-Level Rise on Wave-Dominated Australian Estuaries with Differing Geomorphology. *J. Mar. Sci. Eng.* **2018**, *6*, 66. [CrossRef]
20. Herdman, L.; Erikson, L.; Barnard, P. Storm Surge Propagation and Flooding in Small Tidal Rivers during Events of Mixed Coastal and Fluvial Influence. *J. Mar. Sci. Eng.* **2018**, *6*, 158. [CrossRef]
21. Yu, Y.-C.; Chen, H.; Shih, H.-J.; Chang, C.-H.; Hsiao, S.-C.; Chen, W.-B.; Chen, Y.-M.; Su, W.-R.; Lin, L.-Y. Assessing the Potential Highest Storm Tide Hazard in Taiwan Based on 40-Year Historical Typhoon Surge Hindcasting. *Atmosphere* **2019**, *10*, 346. [CrossRef]
22. Ullman, D.S.; Ginis, I.; Huang, W.; Nowakowski, C.; Chen, X.; Stempel, P. Assessing the Multiple Impacts of Extreme Hurricanes in Southern New England, USA. *Geosciences* **2019**, *9*, 265. [CrossRef]
23. Salehi, M. Storm Surge and Wave Impact of Low-Probability Hurricanes on the Lower Delaware Bay—Calibration and Application. *J. Mar. Sci. Eng.* **2018**, *6*, 54. [CrossRef]
24. Westerink, J.J.; Luettich, R.A.; Blain, C.A.; Scheffner, N.W. ADCIRC: An advanced three-dimensional circulation model for shelves, coasts, and estuaries. report 2. User's manual for adcirc-2ddi. *J. Geol.* **1994**, *76*, 721–723.
25. Westerink, J.J.; Luettich, R.A.; Feyen, J.C.; Atkinson, J.H.; Dawson, C.; Roberts, H.J.; Powell, M.D.; Dunion, J.P.; Kubatko, E.J.; Pourtaheri, H. A Basin- to Channel-Scale Unstructured Grid Hurricane Storm Surge Model Applied to Southern Louisiana. *Mon. Weather. Rev.* **2008**, *136*, 833–864. [CrossRef]

26. Bunya, S.; Dietrich, J.C.; Westerink, J.J.; Ebersole, B.A.; Smith, J.M.; Atkinson, J.H.; Jensen, R.; Resio, D.T.; Luettich, R.A.; Dawson, C.; et al. A High-Resolution Coupled Riverine Flow, Tide, Wind, Wind Wave, and Storm Surge Model for Southern Louisiana and Mississippi. Part I: Model Development and Validation. *Mon. Weather. Rev.* **2010**, *138*, 345–377. [CrossRef]
27. Dietrich, J.C.; Bunya, S.; Westerink, J.J.; Ebersole, B.A.; Smith, J.M.; Atkinson, J.H.; Jensen, R.; Resio, D.T.; Luettich, R.A.; Dawson, C.; et al. A High-Resolution Coupled Riverine Flow, Tide, Wind, Wind Wave, and Storm Surge Model for Southern Louisiana and Mississippi. Part II: Synoptic Description and Analysis of Hurricanes Katrina and Rita. *Mon. Weather. Rev.* **2010**, *138*, 378–404. [CrossRef]
28. Dietrich, J.C.; Westerink, J.J.; Kennedy, A.B.; Smith, J.M.; Jensen, R.E.; Zijlema, M.; Holthuijsen, L.H.; Dawson, C.; Luettich, R.A., Jr.; Powell, M.D.; et al. Hurricane Gustav (2008) Waves and Storm Surge: Hindcast, Synoptic Analysis, and Validation in Southern Louisiana. *Mon. Weather Rev.* **2011**, *139*, 2488–2522. [CrossRef]
29. Dietrich, J.C.; Zijlema, M.; Westerink, J.J.; Holthuijsen, L.H.; Dawson, C.; Luettich, R.A., Jr.; Jensen, R.E.; Smith, J.M.; Stelling, G.S.; Stone, G.W. Modeling hurricane waves and storm surge using integrally-coupled, scalable computations. *Coast. Eng.* **2011**, *58*, 45–65. [CrossRef]
30. Dietrich, J.C.; Tanaka, S.; Westerink, J.J.; Dawson, C.N.; Luettich, R.A., Jr.; Zijlema, M.; Holthuijsen, L.H.; Smith, J.M.; Westerink, L.G.; Westerink, H.J. Performance of the Unstructured-Mesh, SWAN+ADCIRC Model in Computing Hurricane Waves and Surge. *J. Sci. Comput.* **2012**, *52*, 468–497. [CrossRef]
31. Hope, M.E.; Westerink, J.J.; Kennedy, A.B.; Kerr, P.C.; Dietrich, J.C.; Dawson, C.; Bender, C.J.; Smith, J.M.; Jensen, R.E.; Zijlema, M.; et al. Hindcast and validation of Hurricane Ike (2008) waves, forerunner, and storm surge. *J. Geophys. Res. Space Phys.* **2013**, *118*, 4424–4460. [CrossRef]
32. Lin, N.; Emanuel, K.A.; Smith, J.A.; Vanmarcke, E. Risk assessment of hurricane storm surge for New York City. *J. Geophys. Res.* **2010**, *115*, D18121. [CrossRef]
33. Gao, J.; Pan, S.; Wang, H.; Zhang, J.; Tan, X.; Li, C.; Dong, J. Storm surge simulation based on ADCIRC+SWAN coupling model: A case study of the western Shenzhen water. *Mar. Sci. Bull.* **2019**, *38*, 662–674. (In Chinese)
34. NAO.99b Tidal Prediction System. Available online: https://www.miz.nao.ac.jp/staffs/nao99/index_En.html (accessed on 6 May 2023).
35. CMA Tropical Cyclone Data Center for the Western North Pacific Basin. Available online: https://tcdata.typhoon.org.cn/zjljsjj.html (accessed on 6 May 2023).
36. Lu, X.; Yu, H.; Ying, M.; Zhao, B.; Zhang, S.; Lin, L.; Bai, L.; Wan, R. Western North Pacific tropical cyclone database created by the China Meteorological Administration. *Adv. Atmos. Sci.* **2021**, *38*, 690–699. [CrossRef]
37. Integrated Water Level Dataset. Available online: https://mds.nmdis.org.cn/pages/dataViewDetail.html?dataSetId=35 (accessed on 6 May 2023).
38. Dong, J.X.; Fu, X.; Wu, W.; Zhao, L.D.; Yu, F.J. Operational forecast and test of the high resolution numerical storm surge forecast model for China sea. *Mar. Forecast.* **2008**, *25*, 7. (In Chinese)
39. National Catalogue Service for Geographic Information of China. Available online: https://www.webmap.cn/main.do?method=index (accessed on 1 May 2023).
40. Holland, G.J. An Analytic Model of the Wind and Pressure Profiles in Hurricanes. *Mon. Weather Rev.* **1980**, *108*, 1212–1218. [CrossRef]

Disclaimer/Publisher's Note: The statements, opinions and data contained in all publications are solely those of the individual author(s) and contributor(s) and not of MDPI and/or the editor(s). MDPI and/or the editor(s) disclaim responsibility for any injury to people or property resulting from any ideas, methods, instructions or products referred to in the content.